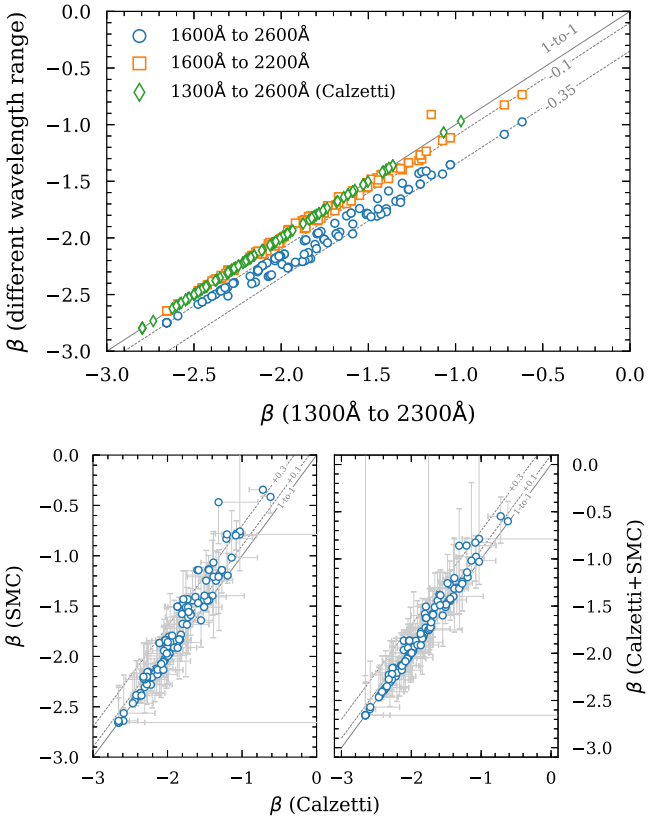

Figure 19. Dependence of UV continuum slope β on the definition of the wavelength regions and assumption of dust attenuation law. The solid line shows the 1–1 relation and the dashed lines show different offsets. Top panel: dependence of β on the adopted wavelength window (with respect to our choice, 1300 Å–2300 Å). Bottom panel: dependence of β on the assumed dust attenuation law. Using an SMC dust attenuation results in redder slopes compared to a Calzetti reddening law.

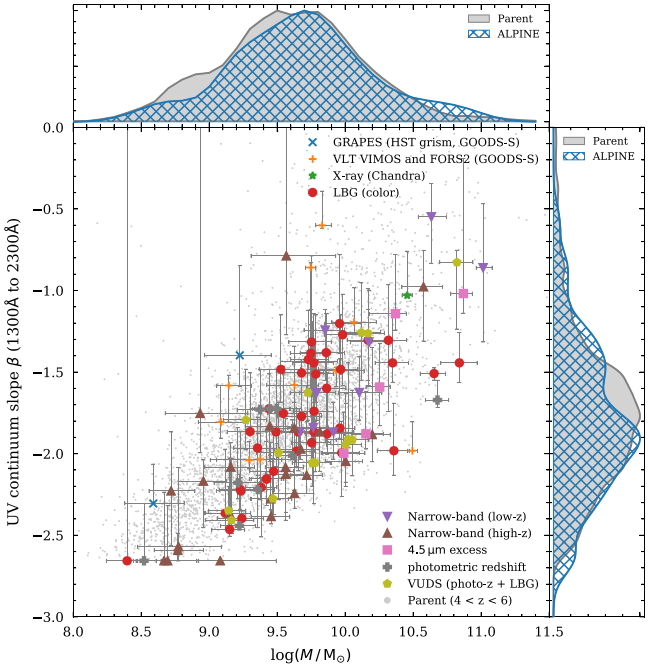

Figure 20. Comparison of UV slopes and stellar mass. The offset panels show kernel density estimates of the β and stellar mass distribution. The ALPINE galaxies (large symbols) are split into their method of selection (see Section 2.1). We also show the data from our parent sample at $4 < z < 5$ (gray dots). Statistically, our ALPINE peaks at ∼0.2 dex higher stellar masses and ∼0.3 bluer β.

ALPINE galaxies would change if different wavelength ranges are used. First, we do not find any differences in our measurements compared to the definition by Calzetti et al. (1994), who use 10 discrete fitting windows between 1300 Å and 2600 Å to avoid strong absorption and emission lines (green diamonds). The other symbols show the comparison to different wavelength ranges, and we notice significant offsets from our measurements. For example, defining β between 1600 Å and 2200 Å results in up to $\Delta\beta = 0.1$ bluer slopes (orange squares). Using a significantly redder wavelength range, 1600 Å to 2600 Å, leads to 0.1–0.35 bluer slopes (blue circles) compared to our definition. Note that the offset varies as a function of β itself—specifically, differences are enhanced toward redder slopes.

The second, more physically driven quantity that affects the measurement of β is the assumed dust attenuation law. As described in Section 4.1.2, the choice of the dust attenuation law has a negligible affect on the stellar masses and SFRs. This is not the case for the β slopes as shown in the lower panels of Figure 19. The left panel compares β derived using Calzetti and SMC dust attenuation. We notice a consistent positive offset of up to $\Delta\beta = 0.3$ for the reddest slopes. We compared the reduced χ^2 values output by `LePhare` for fits using a Calzetti and SMC dust attenuation in order to derive a preference for either of the dust attenuations. We find that the χ^2 values show insignificant differences, which lets us conclude that we are not able to distinguish between the different dust attenuations based on our SED fitting. Hence, we decided that the best way is to be agnostic about the dust attenuation and combine for each galaxy the two probability density functions $P_{\rm Calzetti}(\beta)$ and $P_{\rm SMC}(\beta)$ derived from our Monte Carlo approach (Section 4.3.1) assuming equal weighting to derive the median β and its 1σ uncertainties. In the lower left panel of Figure 19, the final combined β slopes are compared to the β derived assuming a Calzetti attenuation. The offset toward redder β is significantly reduced due to narrower probability density functions, assuming Calzetti dust (hence, the average β is drawn to the Calzetti solution in most cases).

4.3.3. The β Slopes of the ALPINE Galaxies in Context

Figure 20 shows our β measurement (marginalized over both Calzetti and SMC dust) as a function of stellar mass split in the different methods of selection (Section 2.1). As the UV slope is mostly affected by the dust attenuation, the strong correlation between β and stellar mass is not surprising as more massive galaxies are expected to be more dusty. The $z \sim 5.5$ narrowband-selected galaxies, statistically, have the bluest slopes, indicating their dust-poor nature. The other galaxies are spread out over the whole parameter space. We also show the data from our parent sample at $4 < z < 6$ in gray and compare their β slope and stellar mass distribution to the ALPINE sample in the kernel density estimate plots. Note that the β slope distribution of ALPINE galaxies peaks at $\Delta\beta \sim 0.2$ bluer values than the parent sample at the same redshift. This is a minor bias (likely caused by our spectroscopic selection) that has to be kept in mind for future analyses.

Table 4
List of Basis Stellar Population Models for the Parameterization of the Rest-frame Optical Continuum at $4 < z < 5$ to Derive Hα Emission from *Spitzer* Colors

Model	SFH	Metallicity ($Z_\odot = 0.02$)	Dust attenuation
A	Constant	0.02	Calzetti
B	Constant	0.004	Calzetti
C	Exp. declining[a]	0.01	Calzetti
D	Constant	0.02	SMC
E	Constant	0.004	SMC
F	Exp. declining[a]	0.01	SMC

Note.
[a] Assuming $\tau = 3 \times 10^8$ yr.

4.4. Measurement of Hα Emission

Rest-frame optical emission lines in $z > 4$ galaxies are out of reach of current spectrographs. Specifically, the Hα emission provides a good tool to study the star formation properties of galaxies in more detail. Fortunately, in the redshift range $4 < z < 5$, the Hα line falls in the *Spitzer* 3.6 μm filter, while the 4.5 μm filter lacks any strong emission lines. Therefore, the [3.6 μm]−[4.5 μm] color can be used to constrain the Hα line flux and its equivalent width (a proxy of recent stellar mass build up). This method leads to Hα emission properties that are statistically as accurate as derived from spectroscopic data (Faisst et al. 2016a). Several such measurements have been carried out in the past with success (Shim et al. 2011; Stark et al. 2013; de Barros et al. 2014; Smit et al. 2014; Mármol-Queraltó et al. 2016; Faisst et al. 2016a; Rasappu et al. 2016; Smit et al. 2016; Caputi et al. 2017; Faisst et al. 2019).

About 55% of the ALPINE sample (66 galaxies) lie in this redshift range. To measure the Hα luminosity and equivalent widths, we follow the same technique as outlined in Faisst et al. (2019; we refer to this paper for more technical details). In brief, this method makes an assumption on the rest-frame optical continuum to which emission lines are added in a consistent manner to reproduce the observed [3.6 μm]−[4.5 μm] colors of the galaxies. This approach is robust, as it only depends on the slope of the rest-frame optical continuum, which is well defined and nearly independent of assumptions on age, metallicity, and star formation history for galaxies younger than ∼1 Gyr (mostly the case at $z > 4$). To describe the rest-frame optical continuum, we use several basis stellar population models based on the Bruzual & Charlot (2003) template library (see Table 4). For the dust correction of the Hα emission, we assume the stellar $E_s(B-V)$ values derived by `LePhare`, which we convert to nebular extinction factors by assuming an *f*-factor[47] of 0.44 as measured in local starburst galaxies (Calzetti et al. 2000). We also assume a Calzetti and SMC reddening law. Furthermore, we assume an [N II] to Hα ratio of 0.15, as expected for galaxies at $\log(M/M_\odot) = 10$ (Faisst et al. 2018), to correct the blending of the [N II] and Hα lines.

[47] The *f*-factor, $f = E_s(B-V)/E_n(B-V)$, describes the differential dust reddening between the stellar continuum and nebular regions. Its value is largely unknown at $z > 2$, but it is expected that *f* approaches a value closer to unity at higher redshifts (Erb et al. 2006; Reddy et al. 2010; Kashino et al. 2013; Koyama et al. 2015; Valentino et al. 2015; Puglisi et al. 2016; Kashino et al. 2017; Faisst et al. 2019).

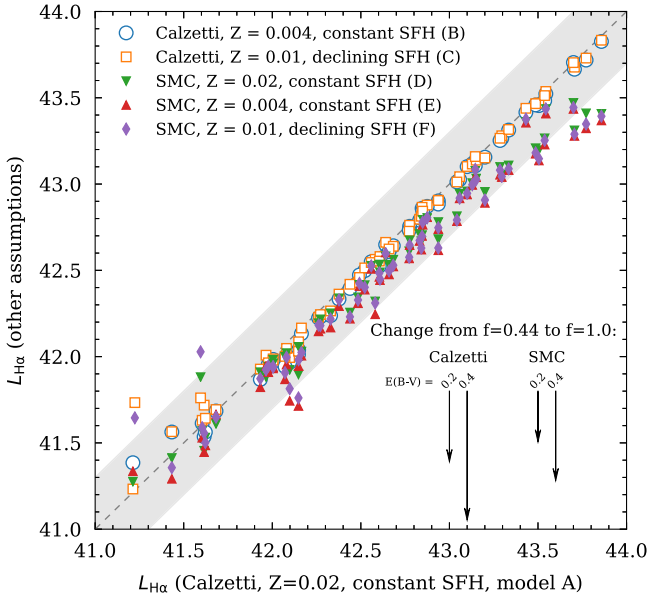

Figure 21. Effect of different assumptions of the rest-frame optical continuum, reddening law, and *f*-factor (arrows show absolute decrease in luminosity from $f = 0.44$–1.0 for different stellar dust attenuations and reddening laws) on the measurement of the Hα luminosity. The gray band shows the 1–1 relation with ±0.3 dex margin. The different models for the continuum are labeled in the same way as in Table 4). The *f*-factor (differential reddening between stellar continuum and nebular regions) has the strongest effect on the Hα luminosity measurements.

In Figure 21, we show systematic uncertainties in the measurement of the Hα luminosity due to the assumptions in our model for the rest-frame optical continuum and the reddening law (models *A* through *F*, see Table 4), as well as the *f*-factor for $E_s(B-V) = 0.2$ and 0.4. It is evident that different assumptions in metallicity and SFH have a negligible impact on the measured Hα luminosity. The choice of the reddening law matters as the Hα luminosity decreases by ∼0.3 dex for galaxies at high Hα luminosities ($\log(L_{H\alpha}/L_\odot) > 43.5$) assuming an SMC reddening law. The *f*-factor is the largest uncertainty in this measurement method and will have to be pinned down by future observations with the JWST. For now, the assumed $f = 0.44$ provides likely an *upper* limit on the Hα luminosities. As shown by the arrows in Figure 21, assuming an *f*-factor equal to unity (which is thought to be more likely based on observations at $z \sim 2$) would decrease the Hα luminosities by up to 0.4 dex (0.8 dex) for a stellar dust reddening of 0.2 (0.4) magnitudes. The correction in the case of an SMC reddening law are 0.1–0.2 dex less. We note that these factors also apply to Hα-derived SFRs and any other quantity that depends linearly on the Hα luminosity.

The top panel of Figure 22 compares the SFRs derived from SED fitting (Section 4.1) to the Hα luminosity and Hα-derived SFRs for galaxies without contaminated *Spitzer* photometry. The latter is derived using the standard conversion factor given in Kennicutt (1998),

$$\mathrm{SFR}(M_\odot\ \mathrm{yr}^{-1}) = 4.5 \times 10^{-42}\, L_{H\alpha}\ (\mathrm{erg\ s}^{-1}), \quad (5)$$

assuming solar metallicity and a Chabrier IMF. Assuming one-fifth solar metallicity, the inferred SFR is expected to be ∼0.2 dex lower (Ly et al. 2016). As shown in Faisst et al. (2019), the uncertainty of this conversion factor is negligible compared to the impact of the uncertain *f*-factor. The Hα luminosities in the ALPINE sample

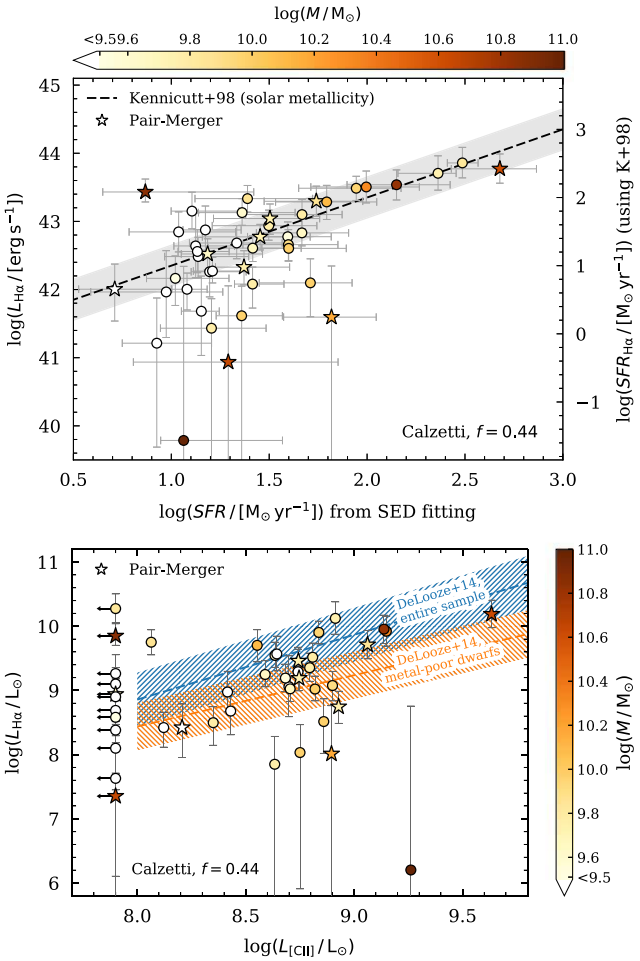

Figure 22. Top panel: comparison of SED-derived SFRs to Hα luminosity (left *y*-axis) and Hα-derived SFR (right *y*-axis). The latter are derived from Hα assuming the conversion factor by Kennicutt (1998) for solar metallicity (dashed line and ±0.3 dex margin, gray). Only galaxies with uncontaminated *Spitzer* photometry are shown. The symbols are color-coded by stellar mass. The star-symbols denote mergers based on the classification in Le Fèvre et al. (2019). The Hα-dependent quantities are derived assuming a Calzetti reddening law, constant SFH, solar metallicity, and $f = 0.44$ (see Figure 21 for effect of different assumptions). Above an SFR of $\sim$13 $M_\odot$ yr^{-1}, the two SFRs are comparable. Below that threshold, the scatter in the Hα-derived SFRs increases due to low S/N of the 4.5 μm observations (see Faisst et al. 2019). Bottom panel: comparison of Hα and [C II] luminosity. Shown are only galaxies with Hα measurements and uncontaminated *Spitzer* photometry. [C II] undetected galaxies (at $<3.5\sigma$) are indicated with upper limits. The lines and dashed margins show the expected relation between Hα and [C II] derived combining the relations from Kennicutt (1998) and De Looze et al. (2014; for their entire sample and metal-poor dwarf galaxies, see the text). Note that at lower [C II] luminosities ($<5 \times 10^8\,L_\odot$), the galaxies seem to be more consistent with the relation of local metal-poor dwarf galaxies.

range from $\sim 10^{41}\,L_\odot$ to $\sim 10^{44}\,L_\odot$ assuming $f = 0.44$ and Calzetti et al. (2000) dust attenuation. The Hα-derived SFRs trace well the SED-derived SFRs above $\sim$13 $M_\odot$ yr^{-1}. Below that value, we see a large scatter in Hα derived SFRs, which happens when the Hα emission becomes too faint to be measured reliably using the *Spitzer* broad bands. Specifically, this is the case roughly at $\log(M/M_\odot) = 9.5$, which corresponds to a 4.5 μm detection of less than 5σ (see Figure 3 and the Appendix in Faisst et al. 2019).

The lower panel of Figure 22 relates the Hα luminosity (here in units of solar luminosity) to the [C II] luminosity measured by ALMA (also solar luminosity). In addition, we show the

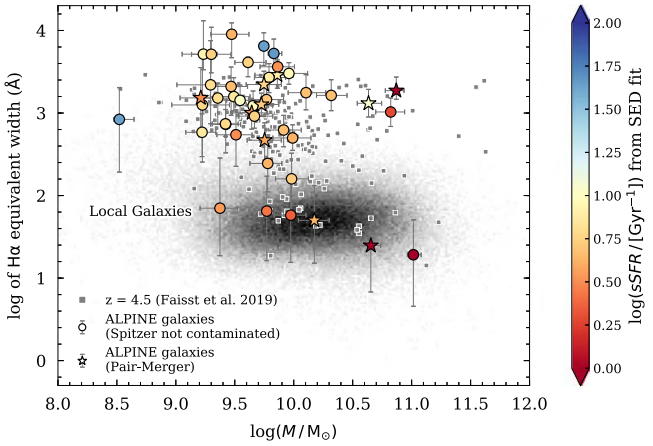

Figure 23. The rest-frame Hα EW of our ALPINE galaxies in context of local galaxies (gray cloud) and $z = 4.5$ galaxies from Faisst et al. (2019) (gray squares). The Hα EW is related to stellar mass and sSFR derived from SED fitting (color-coded). The ALPINE sample at $4 < z < 5$ builds a representative subsample of the general galaxy population at $z > 4$, also in terms of Hα properties. Although with similar stellar masses as local galaxies, the high-redshift galaxies reside at significantly higher Hα EWs, which is naturally explained by their higher star formation. Note the two galaxies with particularly low sSFR (<1 Gyr^{-1}, and consistently low Hα EWs of less than 30 Å) that fall onto the massive end of the distribution of local galaxies. These galaxies are indicative for systems with evolved stellar populations at high redshifts with currently reduced star formation activity.

expected relation between Hα and [C II] luminosity by combining Equation (5) with the linear relation between [C II] and SFR derived by De Looze et al. (2014) from local and low-redshift galaxy samples,

$$\log(\mathrm{SFR} \,/\, [M_\odot\ \mathrm{yr}^{-1}]) = \alpha \times \log(L_{[\mathrm{C\,II}]} \,/\, L_\odot) + \gamma, \qquad (6)$$

for different values of intercepts (γ) and slopes (α). Specifically, we are showing the relation for their entire sample ($\alpha = 1.01$, $\gamma = -6.99$, blue hatched) and the metal-poor dwarf galaxies ($\alpha = 0.80$, $\gamma = -5.73$, red hatched). For bright [C II] galaxies ($L_{[\mathrm{C\,II}]} \gtrsim 5 \times 10^8\,L_\odot$), we find a good agreement with the entire local sample. For lower [C II] luminosities, the Hα measurements fall below this relation and are instead more consistent, although with a large scatter, with the relation of metal-poor local dwarf galaxies. The majority of [C II] undetected galaxies align well with either relation, however, the uncertainty in the Hα measurements becomes substantial as galaxies fall below $\log(M/M_\odot) = 9.5$.

Figure 23 shows the rest-frame Hα EW distribution of our ALPINE galaxies in the context of local galaxies (gray cloud) and other $z \sim 4.5$ galaxies on the COSMOS field (gray, Faisst et al. 2019). The Hα EW for the $z > 4$ galaxies is derived consistently assuming a constant SFH, Calzetti reddening law, and $f = 0.44$. The ALPINE galaxies cover the parameter space of the other $z \sim 4.5$ galaxies and, hence, build a representative sample also in terms of Hα properties. For a fixed stellar mass, the high-redshift galaxies have higher Hα EWs compared to local galaxies, which is expected from a galaxy evolution point of view as galaxies at higher redshift are highly star-forming. Note that two galaxies in the ALPINE sample have similar Hα EW values as massive ($\log(M/M_\odot) > 10.5$) local galaxies. Consistently, also their sSFR are low (<1 Gyr^{-1}), which is

indicative of them being systems with evolved stellar populations at high redshifts.

5. Summary and Conclusions

The early growth phase at redshifts $z = 4$–6 marks an important time in which galaxies build up their stellar mass, enrich in metals and dust, and change their structure to transform into galaxies at the peak of SFR density or thereafter. For a better understanding of this interesting galaxy population, a multiwavelength survey is crucial. ALPINE comprises a valuable set of 118 galaxies at $4.4 < z < 5.9$ with unprecedented ALMA data at $\sim$150 μm FIR wavelengths. Together with the ancillary data presented in this paper, it makes it the first large panchromatic survey to discover the formation and study the evolution of galaxies during the early growth phase.

Summarizing, the science enabling corner stone data sets of ALPINE are:

1. Unprecedented ALMA observations to study the dust, gas, and outflow properties of the largest sample of galaxies to-date at $z > 4$ (Bethermin et al. 2020),
2. Consistently calibrated deep spectroscopic observations at rest-frame UV wavelengths (Section 2) to study Lyα emission and absorption lines (Sections 2.4, 2.4.2),
3. Coherent ground-based (and space-based in ECDFS) imaging data from the optical to near-IR (Section 3) for the measurement of various properties from SED-fitting methods (Section 4.1), including stellar masses and SFRs (Section 4.1.1), UV luminosities (Section 4.2), and UV continuum slopes to study stellar dust attenuation (Section 4.3),
4. Deep *Spitzer* imaging at 3.6 and 4.5 μm to measure Hα emission for 66 galaxies between $4 < z < 5$ (Section 4.4),
5. High-resolution *HST*/ACS imaging in *F*814*W* for all galaxies and WFC3/IR imaging for a smaller fraction (less than 30% with deep *F*160*W* data) to study their resolved structure in connection with FIR [C II] emission (Section 3).

The ALPINE sample is built upon several different selection methods (Section 2.1, Figure 3) and, hence, contains a multitude of different spectroscopic properties. Because of the requirement for spectroscopic confirmation, the sample is slightly biased toward brighter UV magnitudes (Section 4.2, Figure 18) and blue UV continuum slopes ($\Delta\beta \sim 0.2$) compared to the average $4 < z < 6$ galaxy population (Section 4.3, Figure 20). Nonetheless, stellar masses and SFRs, derived from the wealth of ancillary data, show that the ALPINE sample is broadly representative of the $4 < z < 6$ galaxy population.

The FIR [C II] redshifts observed by ALMA allow us to set the systemic redshift of the galaxies in order to study velocity offsets of Lyα emission and several rest-frame UV absorption lines (Section 2.4). From one galaxy at $z = 4.57$ with optical [O III] measurements acquired from Keck/MOSFIRE, we show that the [O III] and FIR [C II] redshifts are in excellent agreement; hence, the latter likely is a good tracer of the systemic redshift derived by optical emission lines at lower redshifts (Section 2.4.3, Figure 11). In general concordance with studies at $z = 2$–3 (using Hα to define the systemic redshift), we find that on average that Lyα is redshifted ($\sim$180 km s^{-1}) with respect to the [C II] line, while the absorption lines are blueshifted (~ -230 km s^{-1}). In Cassata et al. (2020), we perform a more detailed comparison to samples at lower redshifts and study the implication on the Lyα escape fraction in correlation with Lyα equivalent widths. Stacking the spectra in bins of sSFR, we find larger velocity offsets of absorption lines with respect to systemic for galaxies with high sSFRs, which is indicative of stronger winds and outflows in these galaxies (Section 2.4.2, Figure 10). This finding is in agreement with the recent work by Ginolfi et al. (2020), who show a broadening in the FIR [C II] profiles in ALPINE galaxies with high star formation.

Statistically, the SFRs derived from Hα emission via the Kennicutt (1998) relation for galaxies between $4 < z < 5$ agree well with the values derived from SED fitting, assuming a differential dust reddening factor of $f = 0.44$ (Section 4.4, upper panel of Figure 22). However, we observe a considerable scatter for fainter galaxies ($\log(M/M_{\odot}) < 9.5$) due to the lower S/N of the *Spitzer* observations. Thanks to the large sample size of ALPINE, we are able, for the first time, to compare the Hα luminosity to the [C II] luminosity (lower panel of Figure 22). Overall, we find Hα luminosities as expected from the local relation between $L_{[\mathrm{C\,II}]}$ and SFR from De Looze et al. (2014) (using their fit to the entire sample). However, we find that at low [C II] luminosities ($<5 \times 10^8\,L_{\odot}$), the H$\alpha$ luminosities are generally lower than what is predicted by that relation. Instead, the De looze et al. relation derived from a sample of metal-poor dwarf galaxies is a better fit for those galaxies. This might suggest a more complex relation between SFR and [C II] luminosity driven by metallicity or other properties of the ISM.

ALPINE is the beginning of a thorough exploration of galaxies at $z > 4$. It builds the foundation onto which future follow-up observations can build on. In fact, several follow-up programs are being granted, some of which are already on going. These include (i) additional *HST* WFC3/IR observations of interacting ALPINE galaxies (PI: Faisst), (ii) follow-up observations of [N II] at 205 μm with ALMA for nine ALPINE galaxies (PI: Faisst), (iii) high spatial resolution ($\sim$0.″15) observations of the brightest ALPINE galaxies (PI: Ibar), and *(iv)* the follow up of four serendipitous objects at $z > 4$ with NOEMA (PI: Loiacono & Béthermin). In addition, several JWST proposals are in preparation.

All ancillary data products (including catalogs, images, and spectra) will be made public accessible. In Appendix A, we detail the layout of the catalogs including the measurements detailed in this paper. In Appendix B, we show *HST* cutouts in ACS *F*814*W* and WFC3/IR *F*160*W* bands as well as the rest-frame UV spectra of all individual ALPINE galaxies.

This paper completes a series of three papers presenting the ALPINE survey (Le Fèvre et al. 2019) and the data processing (Bethermin et al. 2020).

We would like to thank numerous people for the exchange of data without which the ALPINE ancillary data paper would not exist. In particular, we would like to thank E. Vanzella for helping us gathering the spectra in the ECDFS field and O. Ilbert for useful discussions that improved the SED-fitting results. We also thank the anonymous referee for the suggestions that improved this paper. This paper is based on data obtained with the ALMA Observatory, under Large Program 2017.1.00428.L. ALMA is a partnership of ESO (representing its member states),

NSF (USA) and NINS (Japan), together with NRC (Canada), MOST and ASIAA (Taiwan), and KASI (Republic of Korea), in cooperation with the Republic of Chile. The Joint ALMA Observatory is operated by ESO, AUI/NRAO and NAOJ. This program receives funding from the CNRS national program Cosmology and Galaxies. This work is based on observations and archival data made with the *Spitzer Space Telescope*, which is operated by the Jet Propulsion Laboratory, California Institute of Technology, under a contract with NASA along with archival data from the NASA/ESA *Hubble Space Telescope*. This research made also use of the NASA/IPAC Infrared Science Archive (IRSA), which is operated by the Jet Propulsion Laboratory, California Institute of Technology, under contract with the National Aeronautics and Space Administration. In parts based on data products from observations made with ESO Telescopes at the La Silla Paranal Observatory under ESO programme ID 179.A-2005 and on data products produced by TERAPIX and the Cambridge Astronomy Survey Unit on behalf of the UltraVISTA consortium. Based on data obtained with the European Southern Observatory Very Large Telescope, Paranal, Chile, under Large Program 185.A-0791, and made available by the VUDS team at the CESAM data center, Laboratoire d'Astrophysique de Marseille, France. This work is based on observations taken by the 3D-*HST* Treasury Program (GO 12177 and 12328) with the NASA/ESA *HST*, which is operated by the Association of Universities for Research in Astronomy, Inc., under NASA contract NAS5-26555. Furthermore, this work is based on data from the W. M. Keck Observatory and the Canada–France–Hawaii Telescope, as well as collected at the Subaru Telescope and retrieved from the HSC data archive system, which is operated by the Subaru Telescope and Astronomy Data Center at the National Astronomical Observatory of Japan. The authors wish to recognize and acknowledge the very significant cultural role and reverence that the summit of Maunakea has always had within the indigenous Hawaiian community. We are most fortunate to have the opportunity to conduct observations from this mountain. Finally, we would also like to recognize the contributions from all of the members of the COSMOS Team who helped in obtaining and reducing the large amount of multiwavelength data that are now publicly available through IRSA at http://irsa.ipac.caltech.edu/Missions/cosmos.html. A.C., F.P., M.T., C.G., and F.L. acknowledge the support from grant PRIN MIUR 2017. G.C.J. acknowledges ERC Advanced Grant 695671 "QUENCH" and support by the Science and Technology Facilities Council (STFC). E.I. acknowledges partial support from FONDECYT through grant No. 1171710. The Cosmic Dawn Center (DAWN) is funded by the Danish National Research Foundation under grant No. 140. S.T. acknowledges support from the ERC Consolidator Grant funding scheme (project Context, grant No. 648179). L.V. acknowledges funding from the European Union's Horizon 2020 research and innovation program under the Marie Sklodowska-Curie grant agreement No. 746119. D.R. acknowledges support from the National Science Foundation under grant Nos. AST-1614213 and AST-1910107 and from the Alexander von Humboldt Foundation through a Humboldt Research Fellowship for Experienced Researchers.

Appendix A
Description of Published Data Products

The data presented in this paper are summarized in three different catalogs.

1. The *main catalog*, which contains properties consistently measured for all of the galaxies. These include general information (such as coordinates, redshifts, selection, morphological class), measurements performed on the spectra (such as Lyα redshift and properties as well as absorption line redshifts), measurements from SED fitting (including UV continuum slopes), and Hα line properties and SFRs.
2. The *ECDFS photometry catalog*, which contains all of the Galactic extinction-corrected total photometry (magnitude, fluxes, and uncertainties) of the galaxies in the ECDFS field. This catalog is based on the 3D-*HST* catalog.

Table A1
Column Description of Main Catalog

Column	Unit	Description
		General information and selection
ALPINE_ID	⋯	Unique name for each galaxy in string format
RA	degrees	R.A. in J2000 in degrees from either the COSMOS or 3D-*HST* catalog
delta_RA	milli-arcsec	Constant shift (to be added to RA) in R.A. due to astrometric offset (see Section 3.3)
DEC	degrees	decl. in J2000 in degrees from either the COSMOS or 3D-*HST* catalog
delta_DEC	milli-arcsec	Constant shift (to be added to DEC) in decl. due to astrometric offset (see Section 3.3)
field	⋯	Field name (1 = ECDFS or 2 = COSMOS)
selection	⋯	Original selection. For galaxies in the ECDFS field, this can be *vlt* or *grapes*. For galaxies in COSMOS, possible selections are CHANDRA, *LBG*, *NB1*[a], *NB2*[a], *excess*, *photz*, or *vuds*. See Section 2.1 and Table 1 for details.
z_orig	⋯	Original redshift used for initial selection (this redshift is derived from Lyα or absorption lines).
z_cii	⋯	Redshift determined from FIR [C II] emission lines (see details in Bethermin et al. 2020). Is −99 if [C II] is not detected at S/N > 3.5.
morph_class	⋯	Morpho-kinematic classes from Le Fèvre et al. (2019). Only for galaxies with >3.5σ [C II] detection(else class set to −99). The classes are: (1) rotator; (2) pair-merger (major or minor); (3) extended dispersion-dominated; (4) compact dispersion-dominated; (5) too weak for assigning a class.
		Measurements on spectra (Section 2)
has_twin	⋯	A flag set to 1 of for a galaxy has been observed by Keck/DEIMOS and VUDS (two spectra available). If false, the flag is set to 0.
z_lya	⋯	Redshift determined from peak of Lyα emission (see details in Cassata et al. 2020). Is −99 if no redshift measured.
lya_ew	Å	Observer-frame Lyα emission equivalent (see details in Cassata et al. 2020). Is *−99* if no equivalent width is measured.
lya_ew_err	Å	1σ uncertainty on observer-frame Lyα emission equivalent (see details in Cassata et al. 2020). Is −99 if no equivalent width is measured and −1 if no continuum measured (i.e., EW is upper limit).
f_lya	erg s^{-1} cm^{-2}	Lyα emission flux (see details in Cassata et al. 2020). Is −99 if flux is measured.
flag_specpro	⋯	Visual flag for reliability of absorption redshift measurements. Set to −99 if not attempted, then 1, 2, and 3 for least, medium, and most robust.
z_iswind	⋯	Redshift determined from IS+wind absorption lines (see Section 2.4). Set to −99 if no redshift measured.
z_iswind_low	⋯	Lower 95% percentile of redshift determined from IS+wind absorption lines. Set to −99 if no redshift measured.
z_iswind_up	⋯	Upper 95% percentile of redshift determined from IS+wind absorption lines. Set to −99 if no redshift measured.
n_lines_iswind_used	⋯	Number of lines used for IS+wind redshift measurement. We advise to generally only use galaxies with a value >2 together with flag_specpro >0 for a conservative sample selection.
z_wind	⋯	Redshift determined from wind absorption lines (see Section 2.4). Set to −99 if no redshift measured.
z_wind_low	⋯	Lower 95% percentile of redshift determined from wind absorption lines. Set to −99 if no redshift measured.
z_wind_up	⋯	Upper 95% percentile of redshift determined from wind absorption lines. Set to −99 if no redshift measured.
n_lines_wind_used	⋯	Number of lines used for wind redshift measurement. We advice to generally only use galaxies with a value >0 together with flag_specpro >0 for a conservative sample selection.
		Properties from SED fitting with LePhare (Sections 4.1 and 4.2)
ID_photcat	⋯	ID in the photometric catalogs. This is the 3D-*HST* catalog for galaxies in ECDFS and the COSMOS2015 catalog for galaxies in COSMOS.
chi2	⋯	χ^2 value given by the LePhare fit.
Nband	⋯	Number of bands used for SED fitting.
ebmv	mag	$E(B-V)$ derived from SED fitting.
logAge	yr	Logarithmic age
logAge_loweff1sig	yr	Lower 1σ limit on age in log
logAge_higheff1sig	yr	Upper 1σ limit on age in log
logMstar	$M_\odot$	Logarithmic stellar mass
logMstar_loweff1sig	$M_\odot$	Lower 1σ limit on stellar mass in log
logMstar_higheff1sig	$M_\odot$	Upper 1σ limit on stellar mass in log
logSFR	$M_\odot$ yr^{-1}	Logarithmic SFR
logSFR_loweff1sig	$M_\odot$ yr^{-1}	Lower 1σ limit on SFR in log
logSFR_higheff1sig	$M_\odot$ yr^{-1}	Upper 1σ limit on SFR in log
logsSFR	yr^{-1}	Logarithmic sSFR
logsSFR_loweff1sig	yr^{-1}	Lower 1σ limit on sSFR in log
logsSFR_higheff1sig	yr^{-1}	Upper 1σ limit on sSFR in log
M_FUV	mag	Absolute rest-frame UV magnitude measured in the *GALEX* FUV filter (corresponding approximately to rest-frame 1500 Å)
M_FUV_low1sig	mag	Lower 1σ limit on absolute rest-frame UV magnitude
M_FUV_high1sig	mag	Upper 1σ limit on absolute rest-frame UV magnitude
		UV continuum slopes (β) with different dust reddening (Section 4.3)
beta_med_calz	⋯	UV slope measured assuming Calzetti dust
beta_low1sig_calz	⋯	Lower 1σ UV slope limit (Calzetti dust)
beta_high1sig_calz	⋯	Upper 1σ UV slope limit (Calzetti dust)
beta_med_smc	⋯	UV slope measured assuming SMC dust

Table A1
(Continued)

Column	Unit	Description
beta_low1sig_smc	⋯	Lower 1σ UV slope limit (SMC dust)
beta_high1sig_smc	⋯	Upper 1σ UV slope limit (SMC dust)
beta_med_comb	⋯	UV slope measured by marginalizing over Calzetti and SMC dust
beta_low1sig_comb	⋯	Lower 1σ UV slope limit (Calzetti+SMC dust)
beta_high1sig_comb	⋯	Upper 1σ UV slope limit (Calzetti+SMC dust)
		Hα measurements from *Spitzer* colors (using Model A, see Section 4.4)
spitzer_cont	⋯	*Spitzer* photometry contamination flag. Set to 0, 1, and 2 for no, slight, and heavy contamination, respectively.
ewha_med	Å	Rest-frame Hα equivalent width assuming Calzetti et al. (2000) dust attenuation and $f = 0.44$
ewha_low	Å	Lower 1σ limit of rest-frame Hα equivalent width
ewha_up	Å	Upper 1σ limit of rest-frame Hα equivalent width
log_halum_med	erg s^{-1}	Logarithmic Hα luminosity assuming Calzetti et al. (2000) dust attenuation and $f = 0.44$
log_halum_low	erg s^{-1}	Lower 1σlimit of Hα luminosity in log
log_halum_up	erg s^{-1}	Upper 1σ limit of Hα luminosity in log
log_sfrha_med	$M_\odot$ yr^{-1}	Logarithmic SFR based on Hα luminosity. Derived assuming (Kennicutt 1998) (solar metallicity), Calzetti et al. (2000) dust attenuation, and $f = 0.44$
log_sfrha_low	$M_\odot$ yr^{-1}	Lower 1σ limit of Hα based SFR in log
log_sfrha_up	$M_\odot$ yr^{-1}	Upper 1σ limit of Hα based SFR log

Notes. Sections of this paper where the measurements are discussed are indicated.
[a] Note that *NB1* and *NB2* stand for the narrowband selection of galaxies at $z \sim 4.5$ and $z \sim 5.7$, respectively.

Table A2
Excerpt of the Column Description of the Photometry Catalog for Galaxies in the ECDFS Field (Section 3.1)

Column	Unit	Description
ALPINE_ID	⋯	Unique name for each galaxy in string format
id_3dhst	⋯	Unique identification number in the 3D-*HST* catalog
ra_3dhst	degrees	R.A. as given in 3D-*HST* catalog
dec_3dhst	degrees	decl. as given in 3D-*HST* catalog
Galactic extinction-corrected total fluxes with 1σ uncertainty		
f_f160w	μ *Jy*	*HST*/WFC3 *F*160 flux and uncertainty
e_f160w	μ *Jy*	⋯
⋯	⋯	⋯
Galactic extinction-corrected total magnitudes with 1σ uncertainty		
Note: given are 1σ limits (and magnitude uncertainties are set to -1) if fluxes are smaller than 1σ flux uncertainties.		
mag_f160w	mag	*HST*/WFC3 *F*160 magnitude and error
magerr_f160w	mag	⋯
⋯	⋯	⋯

Note. Wavelengths, depths, and references are given in Table 2.

Table A3
Excerpt of the Column Description of the Photometry Catalog for Galaxies in the COSMOS Field (Section 3.2)

Column	Unit	Description
ALPINE_ID	⋯	Unique name for each galaxy in string format
id_cosmos15	⋯	Unique identification number in the COSMOS2015 catalog
ra_cosmos15	degrees	R.A. as given in the COSMOS2015 catalog
dec_cosmos15	degrees	decl. as given in the COSMOS2015 catalog
Galactic extinction-corrected total fluxes with 1σ uncertainty		
Ks_FLUX_APER3	μ *Jy*	CFHT/WIRCam K_s-band flux and uncertainty
Ks_FLUXERR_APER3	μ *Jy*	⋯
⋯	⋯	⋯
Galactic extinction-corrected total magnitudes with 1σ uncertainty		
Note: given are 1σ limits (and magnitude uncertainties are set to -1) if fluxes are smaller than 1σ flux uncertainties.		
Ks_MAG	mag	CFHT/WIRCam K_s-band magnitude and uncertainty
Ks_MAGERR	mag	⋯
⋯	⋯	⋯

Note. Wavelengths, depths, and references are given in Table 3.

3. The *COSMOS photometry catalog*, which contains all of the Galactic extinction-corrected total photometry (magnitude, fluxes, and uncertainties) of the galaxies in the COSMOS field. This catalog is based on the COSMOS2015 catalog.

The following Tables A1, A2, and A3 summarize the columns of each of these three catalogs. The catalogs can be downloaded in FITS format at http://alpine.ipac.caltech.edu.

Note that the Tables A2 and A3 only show an excerpt of the description of the ECDFS and COSMOS photometry catalog. The full versions can be found at the link above.

Appendix B
Additional Figures

In the following, we show the imaging and spectroscopic data for the individual ALPINE galaxies.

Figures B1–B3 show $2'' \times 2''$ cutouts of the *HST F814W* band of each of the galaxies, sorted by increasing redshift. The redshift, stellar mass, and SFR is indicated. The dashed contours show -3σ levels and the solid contours show 3σ, 5σ, 10σ, 15σ, and 30σ levels. The cutouts are oriented such that north is up and east is to the left. Similarly, Figure B4 and B5

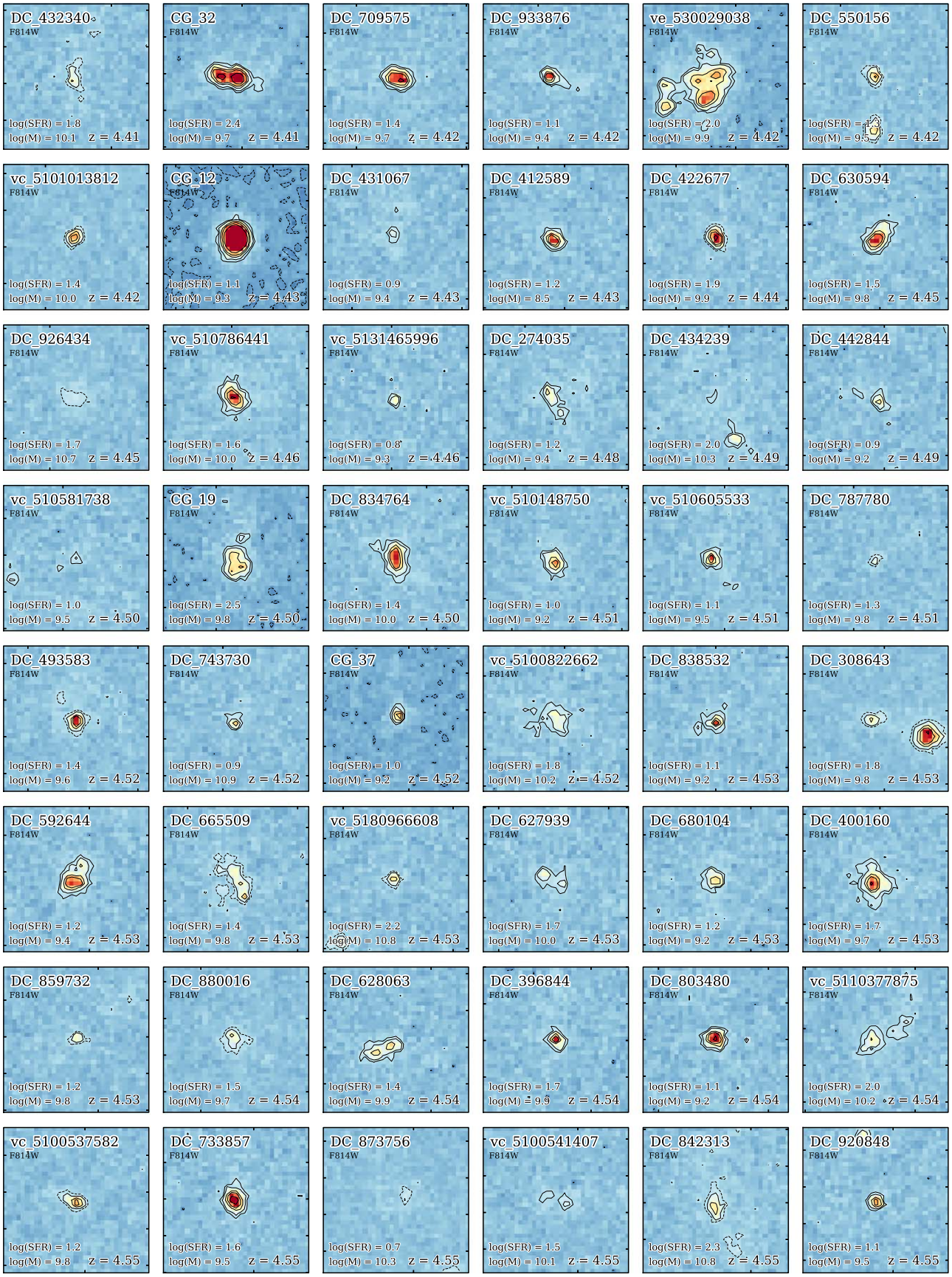

Figure B1. *F*814*W* cutouts sorted by redshift (part 1). The dashed contours show -3σ levels and the solid contours show 3σ, 5σ, 10σ, 15σ, and 30σ levels. All cutouts are $2''$ on each side.

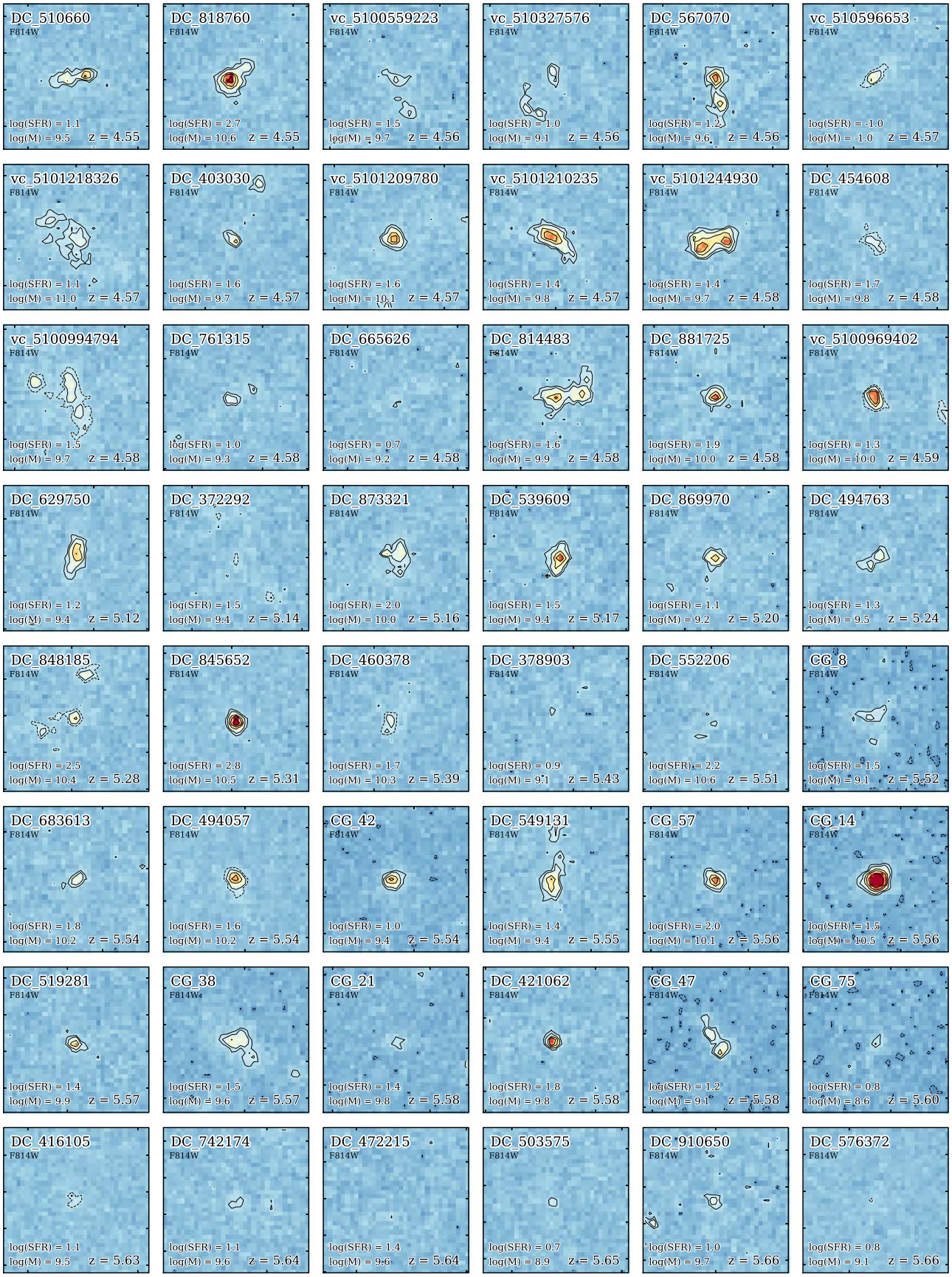

Figure B2. *F*814*W* cutouts sorted by redshift (part 2).

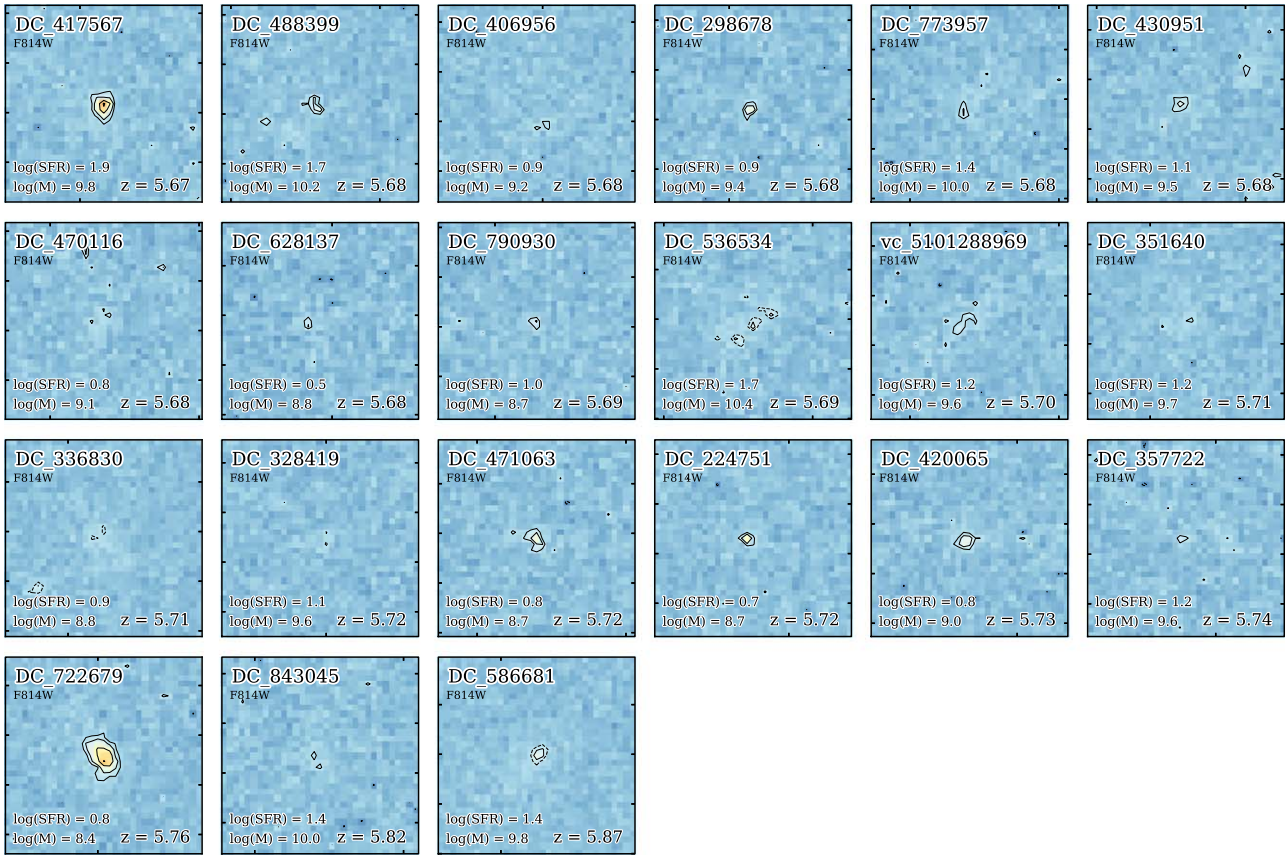

Figure B3. *F*814*W* cutouts sorted by redshift (part 3).

show all of the available *HST F*160*W* data for the ALPINE galaxies as of 2019 October. The cutout size and the drawn σ-levels are the same as in the previous figures. Note that the *HST* program DASH covers most of the galaxies, however, only a fraction is detected due to the low depth of these observations.

Figures B6–B10 show the rest-frame UV spectra for each ALPINE galaxy sorted by increasing redshift. The spectra are smoothed with a Savitzky–Golay filter of size 2 Å. Prominent emission lines as well as individual absorption lines and absorption line complexes are indicated by the dark red bars (compare to Section 2.4.2). For some of the galaxies in COSMOS, a spectrum obtained by VUDS and Keck/DEIMOS is available. The names of these galaxies have an appended "_*v*" or "_*d*," respectively. Note their different spectral resolution.

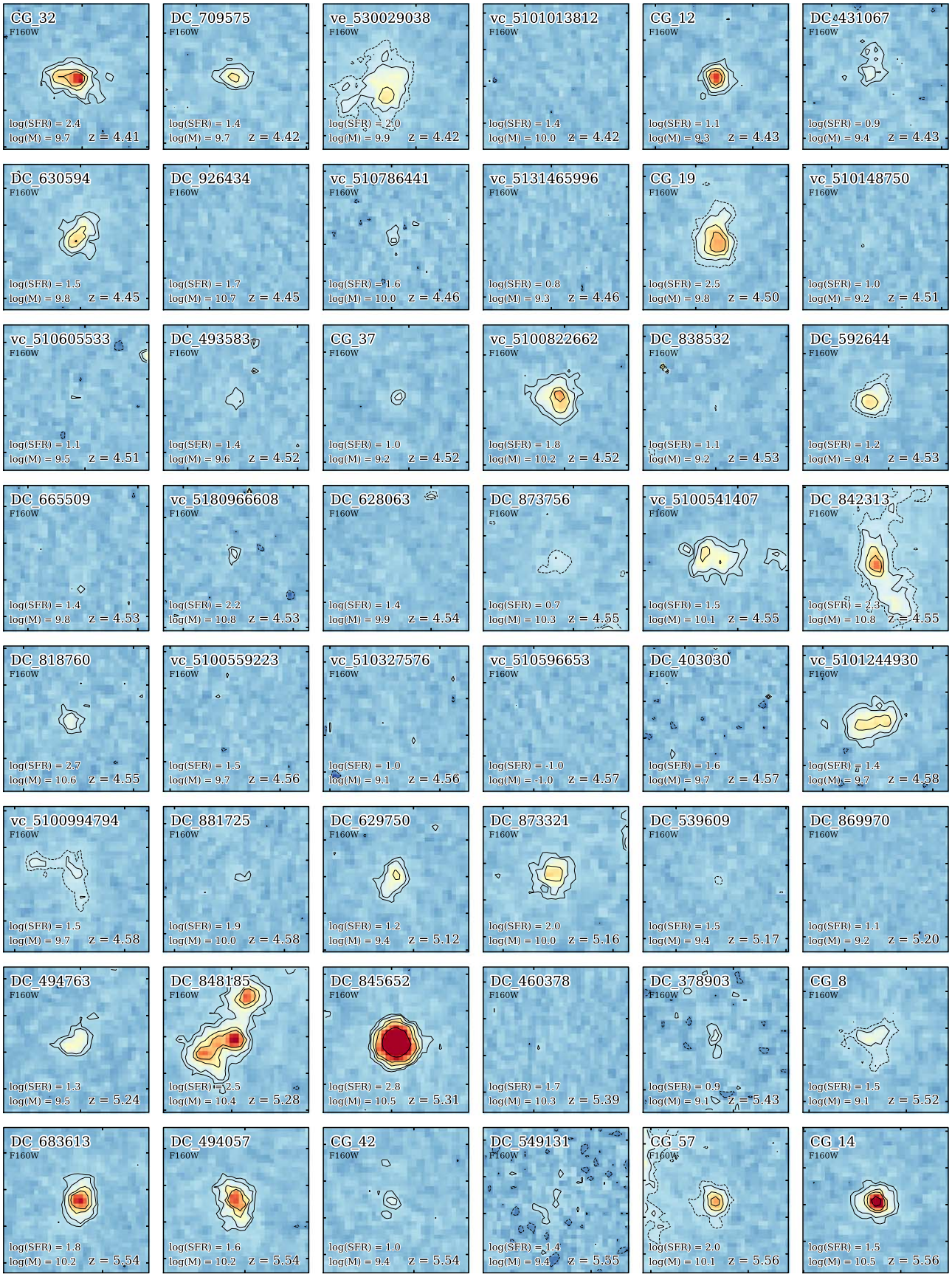

Figure B4. *F160W* cutouts sorted by redshift (part 1). The dashed contours show -3σ levels and the solid contours show 3σ, 5σ, 10σ, 15σ, and 30σ levels. All cutouts are $2''$ on each side.

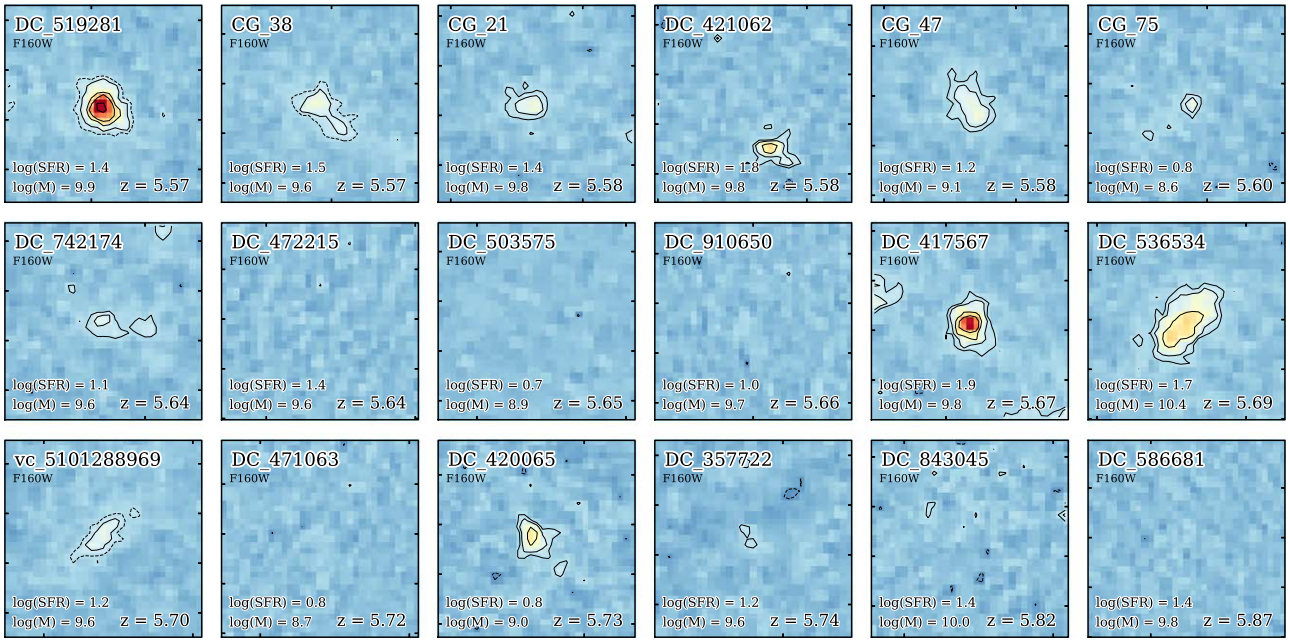

Figure B5. *F160W* cutouts sorted by redshift (part 2).

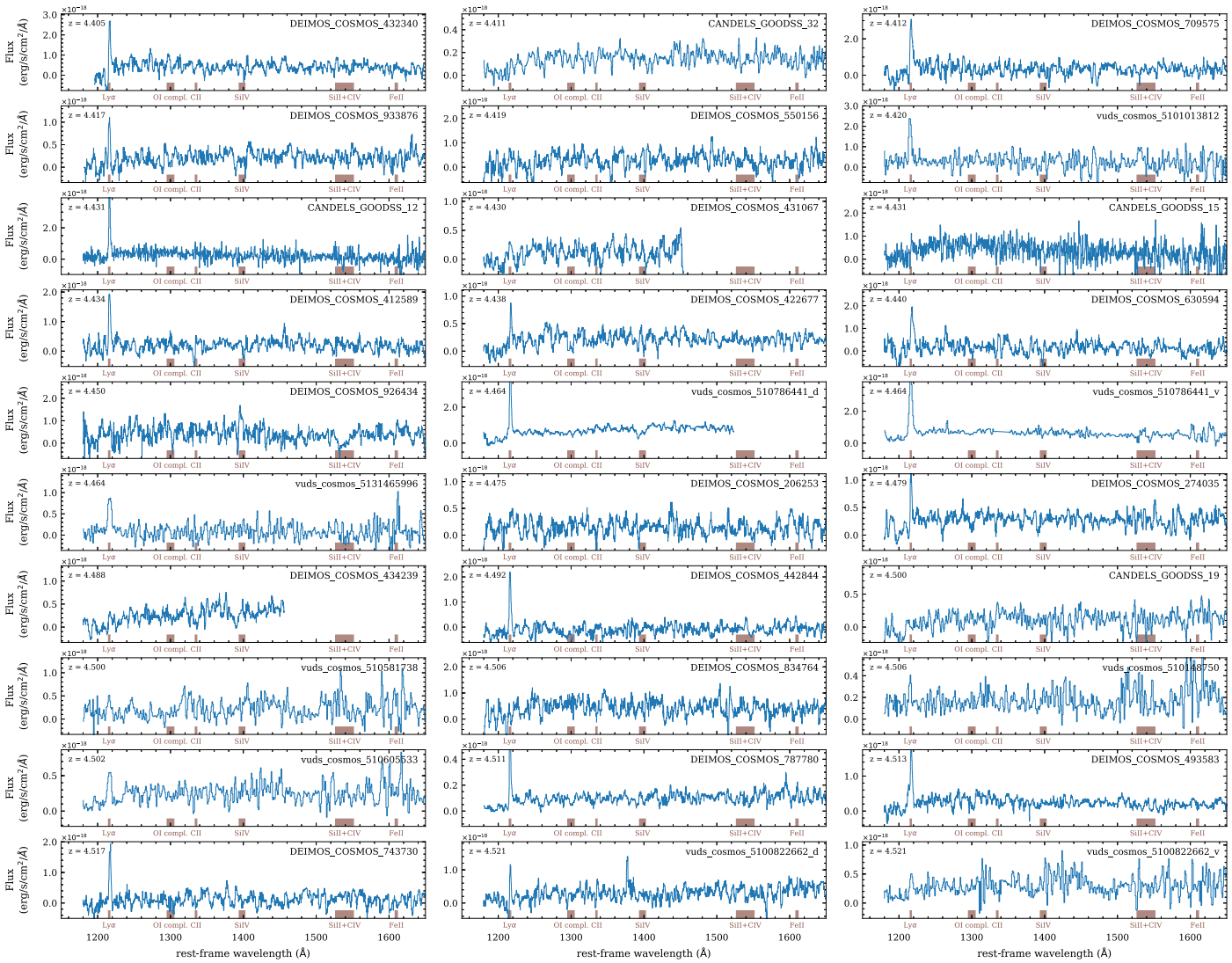

Figure B6. Rest-frame UV spectra of all galaxies sorted by redshift (part 1).

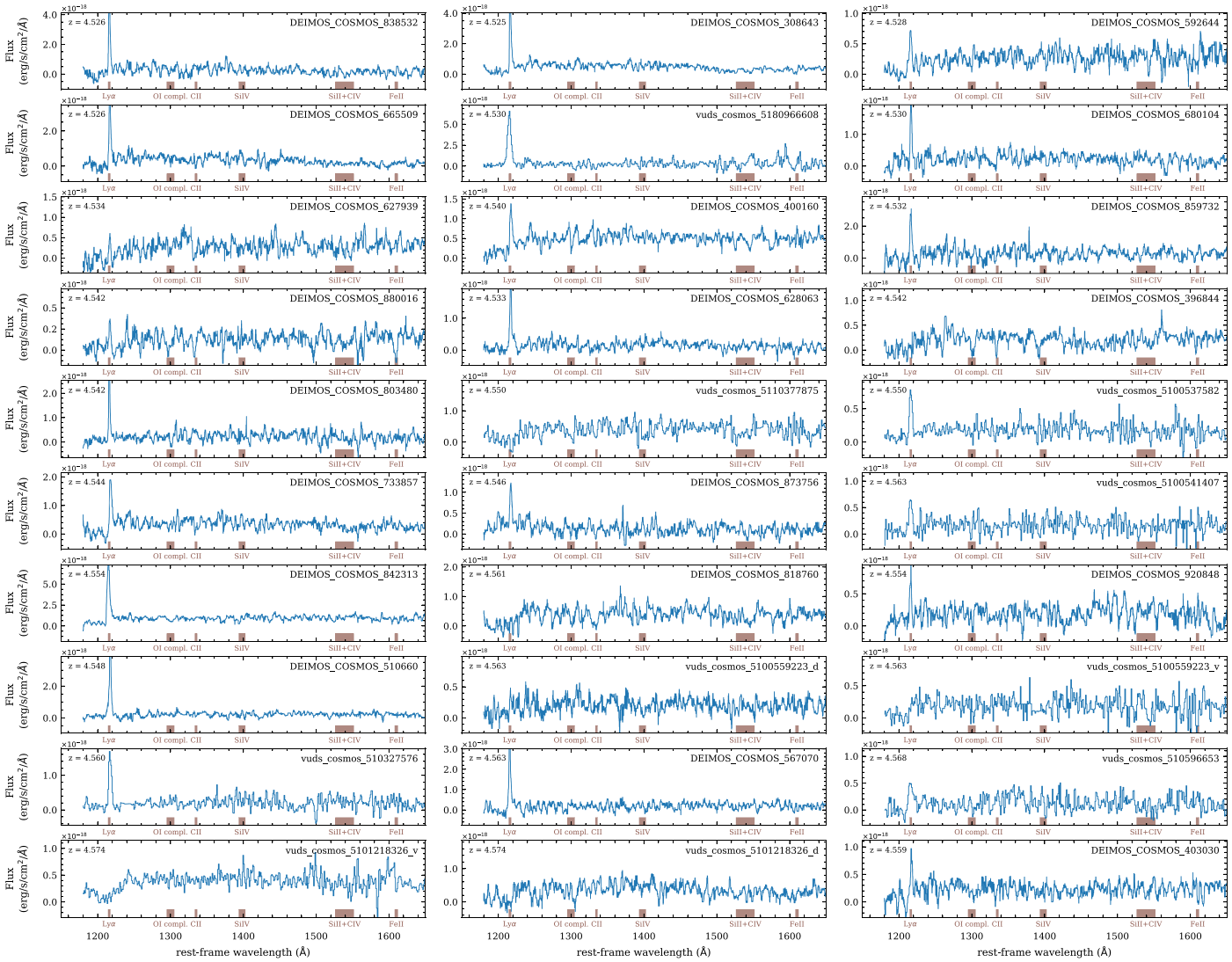

Figure B7. Rest-frame UV spectra of all galaxies sorted by redshift (part 2).

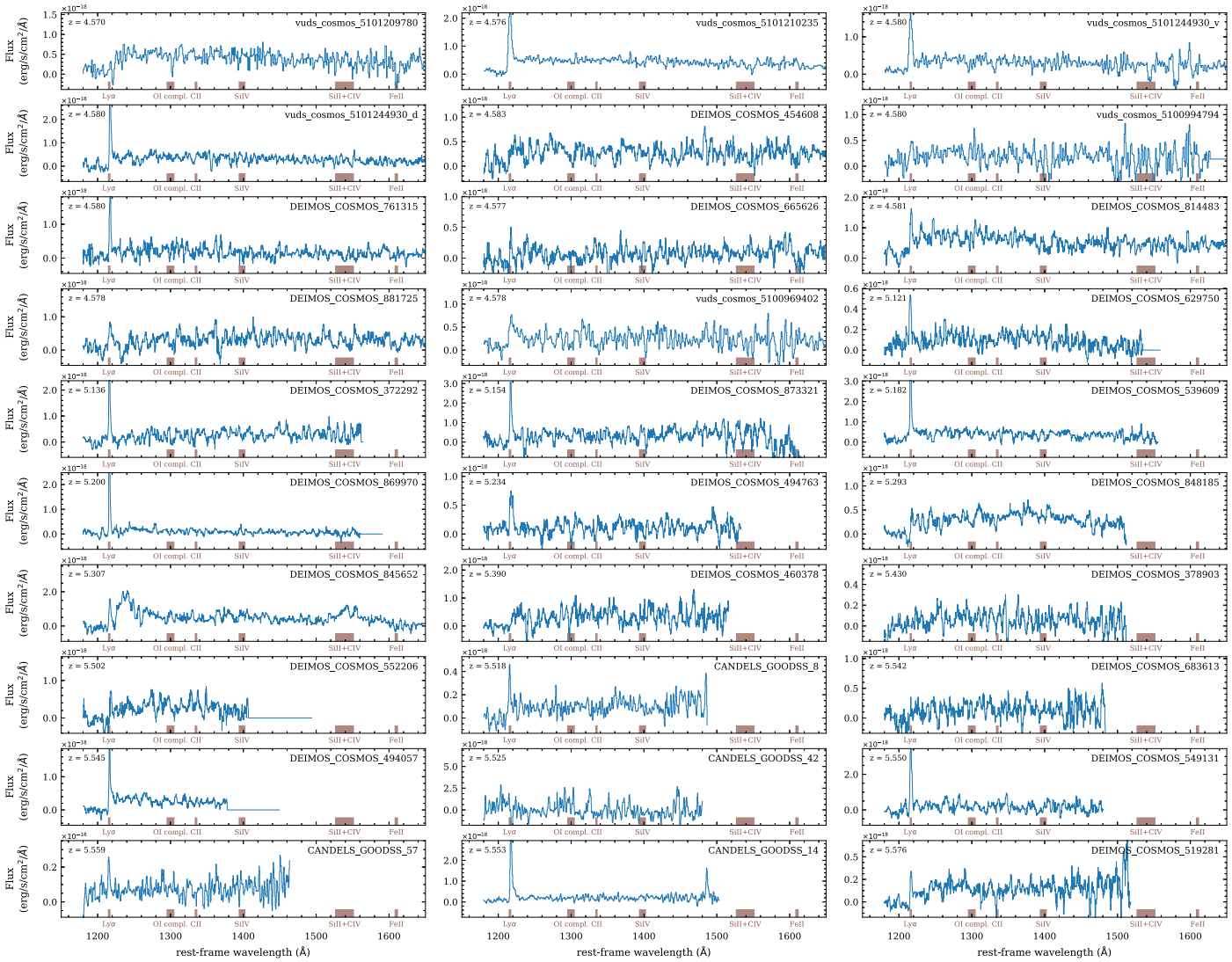

Figure B8. Rest-frame UV spectra of all galaxies sorted by redshift (part 3).

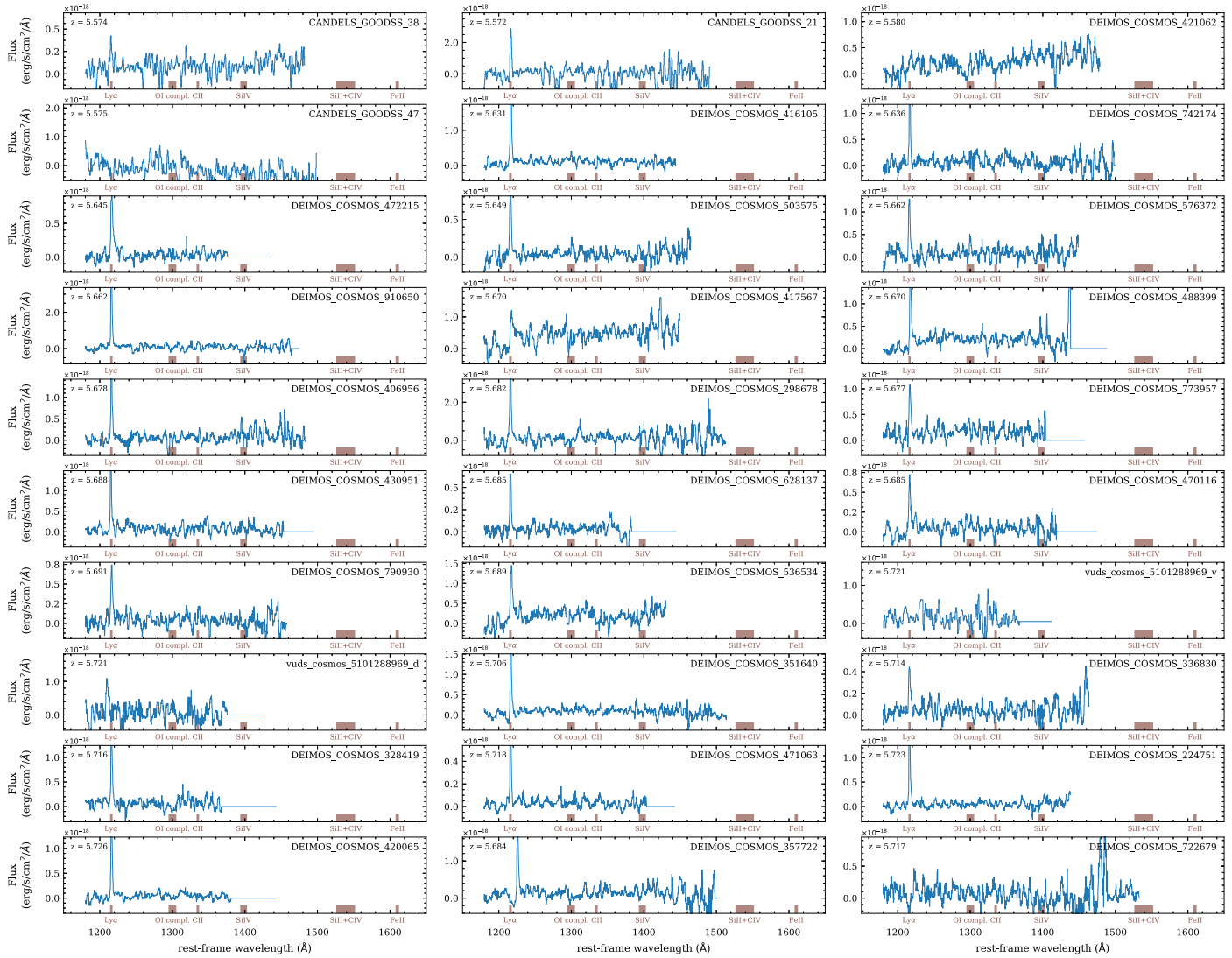

Figure B9. Rest-frame UV spectra of all galaxies sorted by redshift (part 4).

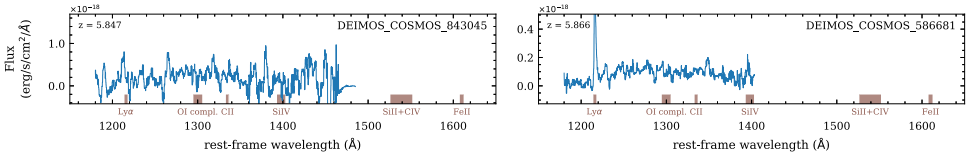

Figure B10. Rest-frame UV spectra of all galaxies sorted by redshift (part 5).

ORCID iDs

A. L. Faisst https://orcid.org/0000-0002-9382-9832
D. Schaerer https://orcid.org/0000-0001-7144-7182
B. C. Lemaux https://orcid.org/0000-0002-1428-7036
P. A. Oesch https://orcid.org/0000-0001-5851-6649
Y. Fudamoto https://orcid.org/0000-0001-7440-8832
P. Cassata https://orcid.org/0000-0002-6716-4400
M. Béthermin https://orcid.org/0000-0002-3915-2015
P. L. Capak https://orcid.org/0000-0003-3578-6843
O. Le Fèvre https://orcid.org/0000-0001-5891-2596
J. D. Silverman https://orcid.org/0000-0002-0000-6977
L. Yan https://orcid.org/0000-0003-1710-9339
A. M. Koekemoer https://orcid.org/0000-0002-6610-2048
R. Amorín https://orcid.org/0000-0001-5758-1000
S. Bardelli https://orcid.org/0000-0002-8900-0298
M. Boquien https://orcid.org/0000-0003-0946-6176
G. Brammer https://orcid.org/0000-0003-2680-005X
A. Cimatti https://orcid.org/0000-0002-4409-5633
M. Dessauges-Zavadsky https://orcid.org/0000-0003-0348-2917
S. Fujimoto https://orcid.org/0000-0001-7201-5066
C. Gruppioni https://orcid.org/0000-0002-5836-4056
N. P. Hathi https://orcid.org/0000-0001-6145-5090
S. Hemmati https://orcid.org/0000-0003-2226-5395
G. C. Jones https://orcid.org/0000-0002-0267-9024
F. Pozzi https://orcid.org/0000-0002-7412-647X
M. Talia https://orcid.org/0000-0003-4352-2063
D. A. Riechers https://orcid.org/0000-0001-9585-1462
G. Rodighiero https://orcid.org/0000-0002-9415-2296
N. Scoville https://orcid.org/0000-0002-0438-3323
S. Toft https://orcid.org/0000-0003-3631-7176
L. Vallini https://orcid.org/0000-0002-3258-3672
G. Zamorani https://orcid.org/0000-0002-2318-301X
E. Zucca https://orcid.org/0000-0002-5845-8132

References

Agertz, O., Teyssier, R., & Moore, B. 2009, MNRAS, 397, L64
Aihara, H., AlSayyad, Y., Ando, M., et al. 2019, PASJ, 71, 114
Ando, M., Ohta, K., Iwata, I., et al. 2007, PASJ, 59, 717
Arnouts, S., Cristiani, S., Moscardini, L., et al. 1999, MNRAS, 310, 540
Ashby, M. L. N., Willner, S. P., Fazio, G. G., et al. 2013, ApJ, 769, 80
Balestra, I., Mainieri, V., Popesso, P., et al. 2010, A&A, 512, A12
Barisic, I., Faisst, A. L., Capak, P. L., et al. 2017, ApJL, 845, 41
Bertin, E., & Arnouts, S. 1996, A&AS, 117, 393
Bethermin, M., Fudamoto, Y., Ginolfi, M., et al. 2020, arXiv:2002.00962
Bolzonella, M., Miralles, J. M., & Pelló, R. 2000, A&A, 363, 476
Bournaud, F., Elmegreen, B. G., & Elmegreen, D. M. 2007, ApJ, 670, 237
Bouwens, R. J., Illingworth, G. D., Franx, M., et al. 2009, ApJ, 705, 936
Bouwens, R. J., Illingworth, G. D., Oesch, P. A., et al. 2014, ApJ, 793, 115
Bouwens, R. J., Illingworth, G. D., Oesch, P. A., et al. 2015, ApJ, 803, 34
Brammer, G. B., van Dokkum, P. G., Franx, M., et al. 2012, ApJS, 200, 13
Bruzual, G., & Charlot, S. 2003, MNRAS, 344, 1000
Calzetti, D., Armus, L., Bohlin, R. C., et al. 2000, ApJ, 533, 682
Calzetti, D., Kinney, A. L., & Storchi-Bergmann, T. 1994, ApJ, 429, 582
Capak, P., Aussel, H., Ajiki, M., et al. 2007, ApJS, 172, 99
Capak, P., Aussel, H., Bundy, K., et al. 2012, sptz prop, 90042
Capak, P., Cowie, L. L., Hu, E. M., et al. 2004, AJ, 127, 180
Capak, P. L., Carilli, C., Jones, G., et al. 2015, Natur, 522, 455
Capak, P. L., Riechers, D., Scoville, N. Z., et al. 2011, Natur, 470, 233
Caputi, K. I., Cirasuolo, M., Dunlop, J. S., et al. 2011, MNRAS, 413, 162
Caputi, K. I., Deshmukh, S., Ashby, M. L. N., et al. 2017, ApJ, 849, 45
Cardamone, C. N., van Dokkum, P. G., Urry, C. M., et al. 2010, ApJS, 189, 270
Carilli, C. L., & Walter, F. 2013, ARA&A, 51, 105
Carniani, S., Maiolino, R., Amorin, R., et al. 2018, MNRAS, 478, 1170
Casey, C. M., Berta, S., Béthermin, M., et al. 2012, ApJ, 761, 140
Casey, C. M., Scoville, N. Z., Sanders, D. B., et al. 2014, ApJ, 796, 95
Casey, C. M., Zavala, J. A., Aravena, M., et al. 2019, ApJ, 887, 55
Cassata, P., Morselli, L., Faisst, A., et al. 2020, arXiv:2002.00967
Castor, J. I., & Lamers, H. J. G. L. M. 1979, ApJS, 39, 481
Chabrier, G. 2003, PASP, 115, 763
Combes, F., Rex, M., Rawle, T. D., et al. 2012, A&A, 538, L4
Cowie, L. L., Barger, A. J., & Hu, E. M. 2011, ApJ, 738, 136
Cullen, F., McLure, R. J., Khochfar, S., et al. 2018, MNRAS, 476, 3218
Davidzon, I., Ilbert, O., Laigle, C., et al. 2017, A&A, 605, A70
de Barros, S., Schaerer, D., & Stark, D. P. 2014, A&A, 563, A81
De Looze, I., Cormier, D., Lebouteiller, V., et al. 2014, A&A, 568, A62
Dickinson, M. 1998, in Proc. STScI Symp., The Hubble Deep Field, ed. M. Livio, S. M. Fall, & P. Madau (New York: Cambridge), 219
Dickinson, M., Giavalisco, M. & GOODS Team 2003, in Proc. ESO Symp., European Southern Observatory and Universitäts-Sternwarte München Workshop, ed. R. Bender & A. Renzini (Berlin: Springer-Verlag), 324
Dunlop, J. S., McLure, R. J., Biggs, A. D., et al. 2017, MNRAS, 466, 861
Egami, E., Rex, M., Rawle, T. D., et al. 2010, A&A, 518, L12
Erb, D. K., Shapley, A. E., Pettini, M., et al. 2006, ApJ, 644, 813
Erben, T., Schirmer, M., Dietrich, J. P., et al. 2005, AN, 326, 432
Faisst, A. L., Capak, P., Hsieh, B. C., et al. 2016a, ApJ, 821, 122
Faisst, A. L., Capak, P. L., Davidzon, I., et al. 2016b, ApJ, 822, 29
Faisst, A. L., Capak, P. L., Emami, N., Tacchella, S., & Larson, K. L. 2019, ApJ, 884, 133
Faisst, A. L., Capak, P. L., Yan, L., et al. 2017, ApJ, 847, 21
Faisst, A. L., Masters, D., Wang, Y., et al. 2018, ApJ, 855, 132
Ferrara, A., Vallini, L., Pallottini, A., et al. 2019, MNRAS, 489, 1
Finkelstein, S. L., Papovich, C., Salmon, B., et al. 2012, ApJ, 756, 164
Franco, M., Elbaz, D., Béthermin, M., et al. 2018, A&A, 620, A152
Fudamoto, Y., Oesch, P. A., Schinnerer, E., et al. 2017, MNRAS, 472, 483
Giacconi, R., Zirm, A., Wang, J., et al. 2002, ApJS, 139, 369
Giavalisco, M., Ferguson, H. C., Koekemoer, A. M., et al. 2004, ApJL, 600, L93
Ginolfi, M., Jones, G. C., Bethermin, M., et al. 2020, A&A, 633, 90
Glazebrook, K., Schreiber, C., Labbé, I., et al. 2017, Natur, 544, 71
Gnedin, N. Y., Norman, M. L., & Ostriker, J. P. 1999, in AIP Conf. Ser. 470, After the Dark Ages: When Galaxies were Young (the Universe at $2 < Z < 5$), ed. S. Holt & E. Smith (Melville, NY: AIP), 48
Grogin, N. A., Kocevski, D. D., Faber, S. M., et al. 2011, ApJS, 197, 35
Gullberg, B., De Breuck, C., Vieira, J. D., et al. 2015, MNRAS, 449, 2883
Guo, Y., Ferguson, H. C., Giavalisco, M., et al. 2013, ApJS, 207, 24
Harikane, Y., Ouchi, M., Shibuya, T., et al. 2018, ApJ, 859, 84
Hashimoto, T., Verhamme, A., Ouchi, M., et al. 2015, ApJ, 812, 157
Hasinger, G., Capak, P., Salvato, M., et al. 2018, ApJ, 858, 77
Heckman, T. M., González-Delgado, R., Leitherer, C., et al. 1997, ApJ, 482, 114
Hildebrandt, H., Erben, T., Dietrich, J. P., et al. 2006, A&A, 452, 1121
Hildebrandt, H., Pielorz, J., Erben, T., et al. 2009, A&A, 498, 725
Hsieh, B.-C., Wang, W.-H., Hsieh, C.-C., et al. 2012, ApJS, 203, 23
Ilbert, O., Arnouts, S., McCracken, H. J., et al. 2006, A&A, 457, 841
Ilbert, O., Capak, P., Salvato, M., et al. 2009, ApJ, 690, 1236
Ilbert, O., McCracken, H. J., Le Fèvre, O., et al. 2013, A&A, 556, A55
Ilbert, O., Salvato, M., Le Floc'h, E., et al. 2010, ApJ, 709, 644
Iwata, I., Ohta, K., Tamura, N., et al. 2003, PASJ, 55, 415
Jin, S., Daddi, E., Magdis, G. E., et al. 2019, ApJ, 887, 144
Jones, G. C., Carilli, C. L., Shao, Y., et al. 2017, ApJ, 850, 180
Kashino, D., Silverman, J. D., Rodighiero, G., et al. 2013, ApJL, 777, L8
Kashino, D., Silverman, J. D., Sanders, D., et al. 2017, ApJ, 835, 88
Kennicutt, R. C., Jr. 1998, ARA&A, 36, 189
Kewley, L. J., & Ellison, S. L. 2008, ApJ, 681, 1183
Khusanova, Y., Le Fèvre, O., Cassata, P., et al. 2020, A&A, 634, 97
Koekemoer, A. M., Aussel, H., Calzetti, D., et al. 2007, ApJS, 172, 196
Koekemoer, A. M., Faber, S. M., Ferguson, H. C., et al. 2011, ApJS, 197, 36
Kohandel, M., Pallottini, A., Ferrara, A., et al. 2019, MNRAS, 487, 3007
Koyama, Y., Kodama, T., Hayashi, M., et al. 2015, MNRAS, 453, 879
Labbé, I., Bouwens, R., Illingworth, G. D., & Franx, M. 2006, ApJL, 649, L67
Laigle, C., McCracken, H. J., Ilbert, O., et al. 2016, ApJS, 224, 24
Lam, D., Bouwens, R. J., Labbé, I., et al. 2019, A&A, 627, A164
Le Fèvre, O., Béthermin, M., Faisst, A., et al. 2019, arXiv:1910.09517
Le Fèvre, O., Tasca, L. A. M., Cassata, P., et al. 2015, A&A, 576, A79
Leitherer, C., Tremonti, C. A., Heckman, T. M., & Calzetti, D. 2011, AJ, 141, 37
Ly, C., Malkan, M. A., Rigby, J. R., & Nagao, T. 2016, ApJ, 828, 67
Ma, X., Hayward, C. C., Casey, C. M., et al. 2019, MNRAS, 487, 1844
Malhotra, S., Rhoads, J. E., Pirzkal, N., et al. 2005, ApJ, 626, 666
Mallery, R. P., Mobasher, B., Capak, P., et al. 2012, ApJ, 760, 128

Maraston, C., Nieves Colmenárez, L., Bender, R., & Thomas, D. 2009, A&A, 493, 425
Marchi, F., Pentericci, L., Guaita, L., et al. 2019, A&A, 631, A19
Mármol-Queraltó, E., McLure, R. J., Cullen, F., et al. 2016, MNRAS, 460, 3587
Masters, D., & Capak, P. 2011, PASP, 123, 638
McCracken, H. J., Milvang-Jensen, B., Dunlop, J., et al. 2012, A&A, 544, A156
McLean, I. S., Steidel, C. C., Epps, H., et al. 2010, Proc. SPIE, 7735, 77351E
McLean, I. S., Steidel, C. C., Epps, H. W., et al. 2012, Proc. SPIE, 8446, 84460J
Meurer, G. R., Heckman, T. M., & Calzetti, D. 1999, ApJ, 521, 64
Mignard, F., & Klioner, S. 2018, in IAU Symp. 330, Astrometry and Astrophysics in the Gaia Sky, ed. A. Recio-Blanco et al. (Cambridge: Cambridge Univ. Press), 71
Mignard, F., Klioner, S., Lindegren, L., et al. 2018, A&A, 616, 14
Momcheva, I. G., van Dokkum, P. G., van der Wel, A., et al. 2017, PASP, 129, 015004
Narayanan, D., Dave, R., Johnson, B., et al. 2018, MNRAS, 474, 1718
Nonino, M., Dickinson, M., Rosati, P., et al. 2009, ApJS, 183, 244
Oke, J. B. 1974, ApJS, 27, 21
Ouchi, M., Shimasaku, K., Okamura, S., et al. 2004, ApJ, 611, 660
Pahl, A. J., Shapley, A., Faisst, A. L., et al. 2020, MNRAS, 493, 3194
Pavesi, R., Riechers, D. A., Capak, P. L., et al. 2016, ApJ, 832, 151
Pavesi, R., Riechers, D. A., Faisst, A. L., Stacey, G. J., & Capak, P. L. 2019, ApJ, 882, 168
Pavesi, R., Riechers, D. A., Sharon, C. E., et al. 2018, ApJ, 861, 43
Pineda, J. L., Langer, W. D., Velusamy, T., & Goldsmith, P. F. 2013, A&A, 554, A103
Popping, G., Somerville, R. S., & Galametz, M. 2017, MNRAS, 471, 3152
Prevot, M. L., Lequeux, J., Prevot, L., Maurice, E., & Rocca-Volmerange, B. 1984, A&A, 132, 389
Puglisi, A., Rodighiero, G., Franceschini, A., et al. 2016, A&A, 586, A83
Rasappu, N., Smit, R., Labbé, I., et al. 2016, MNRAS, 461, 3886
Reddy, N. A., Erb, D. K., Pettini, M., Steidel, C. C., & Shapley, A. E. 2010, ApJ, 712, 1070
Retzlaff, J., Rosati, P., Dickinson, M., et al. 2010, A&A, 511, A50
Rhoads, J. E., Malhotra, S., Pirzkal, N., et al. 2009, ApJ, 697, 942
Riechers, D. A., Carilli, C. L., Capak, P. L., et al. 2014, ApJ, 796, 84
Sanders, D. B., Salvato, M., Aussel, H., et al. 2007, ApJS, 172, 86
Schaerer, D., & de Barros, S. 2009, A&A, 502, 423
Schaerer, D., Ginolfi, M., Bethermin, M., et al. 2020, arXiv:2002.00979
Schlegel, D. J., Finkbeiner, D. P., & Davis, M. 1998, ApJ, 500, 525
Scoville, N., Abraham, R. G., Aussel, H., et al. 2007a, ApJS, 172, 38
Scoville, N., Aussel, H., Brusa, M., et al. 2007b, ApJS, 172, 1
Shapley, A. E., Steidel, C. C., Pettini, M., Adelberger, K. L., & Erb, D. K. 2006, ApJ, 651, 688
Shim, H., Chary, R.-R., Dickinson, M., et al. 2011, ApJ, 738, 69
Skelton, R. E., Whitaker, K. E., Momcheva, I. G., et al. 2014, ApJS, 214, 24
Smit, R., Bouwens, R. J., Labbé, I., et al. 2014, ApJ, 784, 58
Smit, R., Bouwens, R. J., Labbé, I., et al. 2016, ApJ, 833, 254
Speagle, J. S., Steinhardt, C. L., Capak, P. L., & Silverman, J. D. 2014, ApJS, 214, 15
Stacey, G. J., Geis, N., Genzel, R., et al. 1991, ApJ, 373, 423
Stark, D. P., Schenker, M. A., Ellis, R., et al. 2013, ApJ, 763, 129
Steidel, C. C., Erb, D. K., Shapley, A. E., et al. 2010, ApJ, 717, 289
Steidel, C. C., Giavalisco, M., Pettini, M., Dickinson, M., & Adelberger, K. L. 1996, ApJL, 462, L17
Steinhardt, C. L., Speagle, J. S., Capak, P., et al. 2014, ApJL, 791, L25
Stockmann, M., Toft, S., Gallazzi, A., et al. 2020, ApJ, 888, 4
Strandet, M. L., Weiss, A., De Breuck, C., et al. 2017, ApJL, 842, L15
Tanaka, M., Valentino, F., Toft, S., et al. 2019, ApJ, 885, 34
Taniguchi, Y., Kajisawa, M., Kobayashi, M. A. R., et al. 2015, PASJ, 67, 104
Taniguchi, Y., Scoville, N., Murayama, T., et al. 2007, ApJS, 172, 9
Tasca, L. A. M., Le Fèvre, O., Ribeiro, B., et al. 2017, A&A, 600, A110
Valentino, F., Daddi, E., Strazzullo, V., et al. 2015, ApJ, 801, 132
Valentino, F., Tanaka, M., Davidzon, I., et al. 2020, ApJ, 889, 93
Vallini, L., Gallerani, S., Ferrara, A., Pallottini, A., & Yue, B. 2015, ApJ, 813, 36
van Dokkum, P., Brammer, G., Momcheva, I., et al. 2013, arXiv:1305.2140
Vanzella, E., Cristiani, S., Dickinson, M., et al. 2007, in ASP Conf. Ser. 380, Deepest Astronomical Surveys, ed. J. Afonso (San Francisco, CA: ASP), 45
Vanzella, E., Cristiani, S., Dickinson, M., et al. 2008, A&A, 478, 83
Watson, D., Christensen, L., Knudsen, K. K., et al. 2015, Natur, 519, 327
Whitaker, K. E., Ashas, M., Illingworth, G., et al. 2019, ApJS, 244, 16
Whitaker, K. E., Labbé, I., van Dokkum, P. G., et al. 2011, ApJ, 735, 86
Willott, C. J., Carilli, C. L., Wagg, J., & Wang, R. 2015, ApJ, 807, 180
Wuyts, S., Labbé, I., Förster Schreiber, N. M., et al. 2008, ApJ, 682, 985
Wuyts, S., Labbé, I., Franx, M., et al. 2007, ApJ, 655, 51
Yamanaka, S., & Yamada, T. 2019, PASJ, 71, 51
Zavala, J. A., Casey, C. M., da Cunha, E., et al. 2018a, ApJ, 869, 71
Zavala, J. A., Montaña, A., Hughes, D. H., et al. 2018b, NatAs, 2, 56